AGU ADVANCING EARTH AND SPACE SCIENCE

Water Resources Research

RESEARCH ARTICLE
10.1029/2020WR028824

Reconstructing Extreme Precipitation in the Sacramento River Watershed Using Tree-Ring Based Proxies of Cold-Season Precipitation

Swatah Snigdha Borkotoky[1], A. Park Williams[2], Edward R. Cook[2], and Scott Steinschneider[1]

[1]Department of Biological and Environmental Engineering, Cornell University, Ithaca, NY, USA, [2]Tree-Ring Lab, Lamont-Doherty Earth Observatory, Palisades, NY, USA

Key Points:

- Tree-ring based moisture proxies were used to reconstruct extreme precipitation in the Sacramento River Watershed back to 1400 CE
- Tree-ring based proxies in the Intermountain West can improve reconstructions in some years, but can also dampen the magnitude of extremes
- Extreme precipitation was prevalent from 1580 to 1700 and 1850 to 1915, very rare from 1400 to 1550, and exhibited a 2–8 year oscillation after 1550

Supporting Information:

Supporting Information may be found in the online version of this article.

Correspondence to:

S. S. Borkotoky,
sb2499@cornell.edu

Citation:

Borkotoky, S. S., Williams, A. P., Cook, E. R., & Steinschneider, S. (2021). Reconstructing extreme precipitation in the Sacramento River Watershed using tree-ring based proxies of cold-season precipitation. *Water Resources Research*, *57*, e2020WR028824. https://doi.org/10.1029/2020WR028824

Received 18 MAR 2020
Accepted 18 MAR 2021

Abstract Extreme precipitation and consequent floods are some of California's most damaging natural disasters, but they are also critical to the state's water supply. This motivates the need to better understand the long-term variability of these events across the region. This study examines the possibility of reconstructing extreme precipitation occurrences in the Sacramento River Watershed (SRW) of Northern California using a network of tree-ring based moisture proxies across the Western US. We first develop a gridded reconstruction of the cold-season standardized precipitation index (SPI) west of 100°W. We then develop an annual index of regional extreme precipitation occurrences in the SRW and use elastic net regression to relate that index to the gridded, tree-ring based SPI. These regressions, built using SPI data across the SRW only and again across a broader region of the Western US, are used to develop reconstructions of interannual variability in extreme precipitation frequency back to 1400 CE. The SPI reconstruction is skillful across much of the West, including the Sacramento Valley and Central Oregon. The reconstructed SPI also captures historical interannual variations in extreme SRW precipitation, although individual events may be under- or over-estimated. The reconstructions show more SRW extremes from 1580 to 1700 and 1850 to 1915, a dearth of extremes prior to 1550, and a 2–8 year oscillation after 1550. Using tree-ring proxies beyond the SRW often dampens the reconstructed extremes, but these data occasionally help to identify known extreme events. Overall, reconstructions of SRW extreme precipitation can help to understand better the historic variability of these events.

1. Introduction

Water resource management in Northern California is uniquely tied to the occurrence of heavy and extreme precipitation events during the cold season (November to March). These events are not only responsible for major regional floods that threaten the state's water infrastructure (e.g., damaged Oroville Dam spillway in 2017; Vahedifard et al., 2017), but they also constitute over 40% of the annual precipitation total (Dettinger & Cayan, 2014). As temperatures rise and more water from extreme precipitation manifests as early season runoff rather than snowpack (Kapnick & Hall, 2012), it is increasingly important to effectively manage the hazards posed by these events while also capturing runoff for water supply later in the summer. The design and management of infrastructure for this purpose can benefit significantly from an improved understanding of the frequency of extreme precipitation events, including persistence at interannual to decadal time scales (Doss-Gollin et al., 2019). Better quantification of natural variability can also help to contextualize and interpret observed and anticipated trends in extremes due to climate change (Coumou & Rahmstorf, 2012). However, the quantification of extreme precipitation variability is limited by the rarity of these events and relatively short (~100 years) instrumental records. The goal of this study is to reconstruct regional extreme precipitation occurrences in the Sacramento River Watershed (hereafter SRW) for the past several centuries using tree-ring based moisture proxies across the Western US.

Tree-ring widths are not a natural recorder of extreme precipitation events (Fritts, 1966; Meko & Woodhouse, 2010). Tree growth can saturate after enough precipitation has been delivered and moisture availability no longer limits growth. Excess runoff instead of soil moisture recharge and differences in the seasonal timing of tree growth and extremes can also confound the relationship between ring widths and precipitation totals. However, our previous work (Steinschneider et al., 2016) showed that tree-ring based

moisture proxies are strongly related to interannual variability in the frequency of daily extreme precipitation events in much of California, likely because (1) much of the available moisture for tree growth is delivered by a small number of extreme events and (2) cold-season extreme events enhance snowpack that recharges soil moisture throughout the early growing season (Stahle et al., 2020). Dannenberg and Wise (2016) also recently showed that many chronologies across the Western US can capture extreme wet as well as dry water-year precipitation totals. While tree-ring widths cannot capture individual extreme events in the same way as some other paleo-proxies (e.g., paleostage indicators, Benito & Thorndycraft, 2005), our previous work suggests that they can be used in locations like California to infer annual changes in the likelihood of such events over time. Such reconstructions may also be possible in other regions around the world where extreme precipitation contributes significantly to total precipitation and there is a sufficient record of tree-ring chronologies, for example, basins across the western coastline of North America, mid-latitude South America, and the Iberian Peninsula (Gallego et al., 2006; Morales et al., 2020; Natalini et al., 2016; Viale et al., 2018).

The structure and path of storms responsible for extreme precipitation in Northern California further raises the potential to reconstruct the likelihood of these events using tree-ring proxies. Most extreme precipitation events in Northern California are caused by atmospheric rivers (ARs) (Dettinger et al., 2011). ARs are long, narrow, and transient corridors of strong horizontal water vapor transport that are typically associated with a low-level jet ahead of the cold front of an extratropical cyclone (Ralph et al., 2018). When ARs are faced with orographic lift over the Sierra Nevada and Cascades, they can produce some of the most extreme precipitation events in the country (Lamjiri et al., 2017) and can induce significant mudslides and flooding (Ralph et al., 2006).

While not all extreme precipitation events in Northern California are caused by ARs, the association is strong enough so that spatial patterns of precipitation during ARs may bear significantly on the ability to reconstruct extreme precipitation occurrences. The most intense ARs often penetrate past the Sierra Nevada and Cascades through low-elevation corridors, delivering precipitation further into the interior of the Intermountain West (IMW) and particularly the western portion of the IMW (WIMW) (Rutz & Steenburgh, 2012). These low-elevation corridors steer penetrating ARs along preferential pathways, such that the location of their moisture delivery in the WIMW is somewhat predictable given the location of AR landfall along the coast (Alexander et al., 2015; Rutz et al., 2014, 2015; Swales et al., 2016). This presents an opportunity to improve reconstructions of extreme precipitation occurrences along the coast based on precipitation recorded in tree-ring chronologies along those preferential pathways, particularly from moisture-sensitive chronologies in the dry interior of the WIMW. Recently, we demonstrated the promise of this approach for ARs impacting the Southwest US (Steinschneider et al., 2018). In that study, we showed that chronologies across northwestern Arizona, western New Mexico, western Colorado, and central Mexico helped develop robust reconstructions of AR landfalls and extreme precipitation occurrences along the southern California coastline.

It remains unclear if tree-ring based moisture proxies, especially those in the WIMW, can be used to reconstruct extreme precipitation occurrences in Northern California. In the Southwest, chronologies and tree-ring based moisture proxies (particularly those derived from total ring widths) are well suited to isolate cold-season precipitation, since warm-season precipitation delivered by the Southwest Monsoon often evaporates before reaching the root zone (St. George & Ault, 2014; St. George et al., 2010). In the interior of the Pacific Northwest, where many landfalling ARs in Northern California terminate, chronologies exhibit mixed signatures of warm- and cold-season precipitation (Dannenberg & Wise, 2016), complicating the extraction of a cold-season precipitation signal linked to coastal extremes. In addition, the pathways of ARs impacting Northern California are more varied than those in the Southwest US (Alexander et al., 2015). This presents unique challenges not faced in our previous reconstructions of precipitation extremes (Steinschneider et al., 2018).

Given the above knowledge gap, this study seeks to answer the following questions:

1. Can tree-ring based moisture proxies be used to reconstruct the likelihood of regional extreme precipitation occurrences across the SRW?
2. Do tree-ring based data outside of the SRW, such as elsewhere along the West Coast or in the WIMW, improve our reconstruction of extreme precipitation occurrences in the SRW?

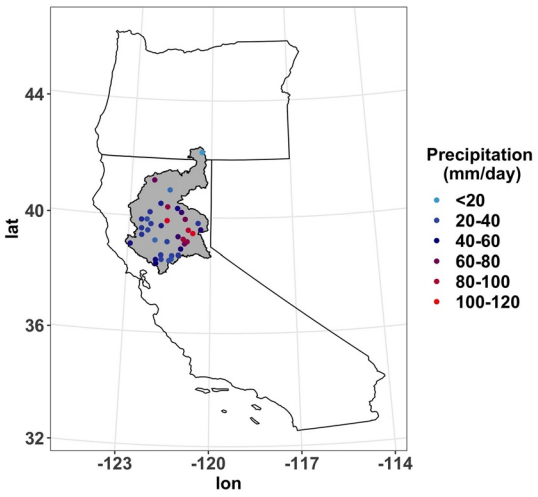

Figure 1. The extreme precipitation threshold (99.5th percentile of daily precipitation in mm/day) at 37 stations across the Sacramento River Watershed (SRW).

To answer these questions, we first develop a gridded, tree-ring based reconstruction of cold-season precipitation across the Western US. We then use this product to reconstruct an index of cold-season extreme precipitation frequency in the SRW. We assess model skill to help identify the benefits and weakness across two model formulations with different spatial domains, and then examine the variability of SRW extreme precipitation back to 1400 CE.

2. Data

2.1. Precipitation

The station-based Global Historical Climatology Network (GHCN; Menne et al., 2012) forms the primary source of daily precipitation data used in this study. As a first step, any missing daily precipitation total is marked as zero if all other stations within 50 km with valid precipitation measurements that day reported zero precipitation. This data set is then used to gap fill a subset of stations within the SRW (Hydrologic Unit Code of 1802). These selected stations had, prior to gap filling, at least 75% of daily values in at least half of all calendar months during at least three of the four 26-year sub-periods over the period January 1, 1915–March 31, 2020 (final period is 17.25 years). Thus, gap filling is only applied to stations that already had good data coverage throughout 1915–2020. The gap-filling procedure is based on a quantile mapping approach using nearby stations, and is described in detail in Text S1. After gap-filling, we ultimately retain 37 stations in the SRW (Figure 1) with non-missing daily values on at least 95% of days in each of the four sub-periods during 1915–2020.

In addition to the primary, gap-filled station-based data set above, we also employ two other gridded precipitation data sets. First, a long record (1895–2018) of monthly precipitation observations are taken from the 1/24° NOAA Climgrid data set in the continental United States (Vose et al., 2014) and the 0.5° CRU 4.04 data set in southern Canada and northern Mexico (Harris et al., 2014) to support the cold-season precipitation reconstruction. We aggregate the NOAA Climgrid data to a 0.5° geographic resolution and truncate to begin in 1901 for consistency with CRU 4.04. Second, we use daily gridded precipitation data available over a shorter period (1950–2013; Livneh et al., 2015) in a diagnostic analysis of extreme events. This product has a 6 × 6 km resolution and is scaled on a monthly basis to match the long-term mean PRISM data (Daly et al., 1994), which takes into account the extreme topography in the Western US.

2.2. Tree-Ring Chronologies

For the cold-season precipitation reconstruction we use the same network of western North American tree-ring records used by Williams et al. (2020a), which is an update of the network used for previous hydroclimate reconstructions in western North America (Cook et al., 2010b; Stahle et al., 2020; Williams et al., 2020b). The network is composed of 1,620 chronologies of ring-width index (RWI) from the western North American domain of 24°N-56°N, 102°W-124°W and have continuous data coverage for at least 1800–1983. Of these chronologies, 1,458, 866, 483, and 332 chronologies extend back to 1700, 1600, 1500, and 1400, respectively. An RWI chronology is an average record of standardized annual tree-ring widths that have been detrended to remove biological growth trends unrelated to climate (Fritts, 1976). The RWI chronologies are calculated from raw tree-ring width measurements, mostly obtained from the International Tree-Ring Databank hosted by NOAA. All chronologies for which the raw ring measurements were available are detrended using the state-of-the-art "signal-free" method, designed to preserve maximal decadal-to-centennial growth variability common among individual tree-ring records and therefore due to climate (Melvin & Briffa, 2008). These methods are discussed further in other recent publications (Cook et al., 2015; Williams et al., 2020b).

3. Methodology

We first develop a gridded reconstruction of cold-season precipitation across the Western US (west of 100°W meridian), which will provide a spatially and temporally complete data set of covariates to predict extreme precipitation occurrences in the SRW. We then use an initial set of diagnostics over the instrumental record to establish the observed spatial patterns of daily precipitation anomalies across the Western US during events that deliver extreme daily precipitation in the SRW. Daily extreme events in the SRW are then aggregated into a basin-wide cold-season index of regional extreme precipitation occurrences. Penalized regression is used to relate this index to the gridded reconstruction of cold-season precipitation over two different spatial domains in a cross-validated framework to determine whether paleo-proxy data from the coastal region and continental interior can support a reconstruction of SRW extremes. We use the regression models to reconstruct the index of SRW extremes back to 1400 CE.

3.1. Reconstruction of Cold-Season Precipitation Across the Western US

We use the Climgrid-CRU monthly precipitation data set to develop a new gridded 0.5°-resolution reconstruction of the 5-month standardized precipitation index (SPI; Guttman, 1999; McKee et al., 1993) for the cold-season (November to March) across the Western US between 1902 and 2018. The SPI expresses cold-season precipitation totals as standardized anomalies after the data have been normalized. Our reconstruction is a direct extension of the SPI reconstruction developed by Williams et al. (2020a) and is similar to one produced by Stahle et al. (2020), but ours (and that of Williams et al., 2020a) incorporates a number of new RWI chronologies, including new precipitation-sensitive chronologies in the northern Sierra Nevada (Lepley et al., 2020). Our reconstruction also retains a higher effective spatial resolution (described below), which is important to our goal of detecting nuanced spatial signatures of regional precipitation events.

The SPI reconstruction is developed using the general point-by-point principal-components regression approach used for many other gridded hydroclimate reconstructions (Cook et al., 2010a; Cook et al., 1999; Cook et al., 2010b; Cook et al., 2015; Cook et al., 2004; Palmer et al., 2015; Stahle et al., 2020; Stahle et al., 2016; Williams et al., 2020b). We develop an ensemble of reconstructions with various combinations of search radii (the maximum distance between tree-ring chronologies and the center of the reconstruction grid cell was allowed to vary from 25 to 250 km), spatial smoothing of the target field (locally averaged SPI in a 0.5°, 1.5°, or 2.5° box around each 0.5° grid cell), and calibration period (water years 1902–1983, 1990, 1995, 2000, or 2005). Our search radii of 25–250 km are small relative to the search radii of 500 and 1,000 km used in Stahle et al. (2020), reflecting our prioritization of spatial resolution over high skill in areas with few precipitation-sensitive RWI chronologies. In the final SPI reconstruction, we allow these parameters (i.e., combination of search radius, target smoothing, and calibration period) to be selected by grid cell so that each reconstruction yields the best verifying reconstruction over the maximum length of time. Our reconstruction differs from that in Williams et al. (2020a) because we allow for multiple calibration periods to be considered; Williams et al. (2020a) only used 1902–2000.

The specific combination of calibration period, search radius, and spatial resolution of observations selected for each grid cell is determined with a *k*-folds (leave-9-years-out) cross-validation approach. Validation reconstruction models are iteratively reproduced by withholding all sets of 9 consecutive years from the calibration period and reconstruction estimates are made for the withheld years until the full original calibration period is represented by out-of-sample reconstruction estimates. The best verifying reconstruction is determined by relating the full calibration period's time series of out-of-sample reconstruction estimates to observations, based on the Akaike Information Criterion (Akaike, 1974; Hurvich & Tsai, 1989). Final reconstruction skill is reported as the cross-validated R^2 between calibration-period observations and the corresponding out-of-sample estimates.

Our reconstruction is developed in a nested approach, where even though the reconstruction extends back to 1400 CE, it takes advantage of the many RWI chronologies that do not extend back that far. For a given grid cell, we initially reconstruct only for the period common to all available tree-ring records within the search radius (e.g., back to 1750). Then, the shortest tree-ring record is dismissed and the reconstruction process is repeated on the new common period among remaining tree-ring records (e.g., back to 1720), and

the original reconstruction is then extended backwards with the new reconstruction values (in this case 1720–1749).

The final gridded SPI reconstruction provides a spatially and temporally complete data set of covariates that can be used to reconstruct extreme precipitation occurrences in the SRW (see Section 3.3). The spatially complete nature of the data also allows us to identify spatial patterns in the tree-ring record that best relate to extreme precipitation in the SRW.

3.2. Diagnostic Assessment of Western US Precipitation During Northern California Extremes

Our primary goal is to reconstruct the interannual variability of extreme precipitation frequency in the SRW based on reconstructed cold-season SPI across the Western US. To better understand the potential for such a reconstruction, we explore the observed (i.e., instrumental record based) space-time characteristics of precipitation anomalies across the Western US during and immediately after extreme precipitation events in the SRW. The goal is to understand how storms linked to SRW extremes of varying intensity influence precipitation over a broader spatial domain, which could be recorded in tree-ring chronologies over that broader domain and thus used to support reconstructions of SRW extremes.

This analysis is conducted using data for cold seasons from 1951 onward when daily gridded data are available across the Western US (Livneh et al., 2015). Extreme precipitation days based on the gap-filled GHCN product in the SRW are initially defined using criteria to isolate large-scale extremes that affected many stations in the basin. In particular, extreme precipitation days are defined as those days when more than 5%, 10%, 20%, or 30% of the stations in the SRW exceed their 99.5th percentiles (defined using cold-season days with both zero and non-zero precipitation). This classification results in four separate (and nested) sets of extreme precipitation days. These sets are then culled to ensure they represent mutually exclusive sets of days. That is, the days based on the 30% threshold are removed from the days based on the 20%, 10%, and 5% thresholds, the days based on the 20% threshold are removed from the days based on the 10% and 5% thresholds, and so on. Then, for each of the four mutually exclusive sets of days, extreme precipitation days are clustered into events, such that an event can consist of multiple days. If four or fewer non-extreme days fall between two extreme precipitation days, then all days in that sequence are considered part of the same event. Each event is then extended 2 days beyond the last extreme precipitation day of that event to account for the time required for ARs and other storms to penetrate inland.

For each set of mutually exclusive events defined using the GHCN data in the SRW, we characterize precipitation anomalies across the entire Western US using two metrics and the gridded Livneh data (Livneh et al., 2015). These metrics include (1) the percentage of total cold-season precipitation between 1951 and 2013 for each Livneh grid cell that occurred on days associated with SRW extreme events (as defined above) and (2) the minimum precipitation for each Livneh grid cell that occurred during those SRW extreme events (expressed as a fraction of the daily average precipitation). We also examine the percentage of total cold-season precipitation (i.e., the first metric) associated with SRW extreme events inclusively across all sets of events (i.e., not separated by the four thresholds). The first metric helps to determine locations across the US West Coast and WIMW that receive significant percentages of total precipitation from storms that are associated with SRW extremes. The second metric helps identify locations that always receive some precipitation during SRW extremes, ensuring that the percentages given by the first metric are driven by all storms associated with SRW extremes rather than just a subset of events. Tree-ring chronologies near locations that meet both of these criteria are more likely to record SRW extreme events, as such events consistently and significantly influence precipitation at those locations.

3.3. Reconstruction of Regional SRW Extreme Precipitation Occurrences

3.3.1. Annual Regional Extreme Occurrence (AREO) Index

The diagnostic assessment in Section 3.2 uses somewhat arbitrary thresholds to provide an intuitive assessment of how precipitation across the Western US varies as extreme precipitation in the SRW becomes more regional in nature. Here, we define an index of annual regional extreme occurrence (the AREO) that represents the total annual count of extreme event days during the cold season across all 37 stations in the

SRW, which is used in our final reconstructions of extreme precipitation frequency. The AREO is calculated for each cold season simply by summing up the total number of times each of the 37 stations exceeds its 99.5th percentile in that year. The index captures regional extreme events because it increases as more stations across the region experience extreme precipitation days. The AREO has the benefit of avoiding the need to select a number of stations exceeding the 99.5th percentile threshold in order to define a regional extreme event day.

3.3.2. Penalized Poisson Regression

After deriving the annual AREO index, we use a penalized Poisson regression to reconstruct the index using data in different spatial domains of the SPI reconstruction:

$$P\left(\mathrm{AREO}_i = z\right) = \frac{\lambda_i^z e^{-\lambda_i}}{z!} \tag{1}$$

$$\log \lambda_i = \beta_0 + x_i^T \beta \tag{2}$$

Here, x_i is a K-dimensional column vector of tree-ring based SPI across K grid cells for the ith year (x_i^T is the transpose), λ_i is the mean estimate for the AREO in year i, and β is a K-vector of regression coefficients. As is common in a Poisson regression, λ_i is log-transformed to ensure non-negativity in the count-based response variable (i.e., AREO). Uncertainty around the AREO reconstruction in each year is characterized using the fitted Poisson distribution.

We use a penalized Poisson regression to account for the high multi-collinearity between the grid cells of the SPI product. In particular, we use elastic net regression (Zou & Hastie, 2005), which is a balance between ridge regression (Hoerl & Kennard, 1970) and Least Absolute Shrinkage and Selection Operator regression (LASSO, Tibshirani, 1996). The elastic net regression is fit by minimizing the negative log-likelihood function $l\left(\beta \mid \mathrm{AREO}, X\right)$ subject to a penalty on the fitted regression coefficients β:

$$\arg\min_{\beta} -\frac{1}{N} l\left(\beta \mid \mathrm{AREO}, X\right) + \gamma\left(\frac{\left(1-\alpha\right)}{2} \parallel \beta \parallel_2^2 + \alpha \parallel \beta \parallel_1\right) \tag{3}$$

Here, $\parallel \beta \parallel_2$ and $\parallel \beta \parallel_1$ are the Euclidean and Manhattan norms of β, respectively, γ and α are penalization hyperparameters. The parameter γ controls the degree of regularization, while α determines the weighting between the type of penalty (ridge vs. LASSO). Elastic net promotes group selection, that is, the inclusion or exclusion of groups of strongly correlated variables in the model. This penalization approach helps to avoid over-fitting but retains groups of potentially important predictors instead of arbitrarily assigning the effect to a single variable (as in LASSO). Still, elastic net regression tends to select a sparse number of covariates among the original set. The two penalization hyperparameters are selected using a 10-fold cross validation. The model is fit using the glmnet package in R.

3.3.3. Intermodel Comparison and AREO Reconstruction

We fit two separate Poisson regression models using two spatial domains of SPI covariates. The first domain consists of SPI grid cells only in the SRW (hereafter SRW-only). The second domain consists of grid cells in five states along the Western US coast and the WIMW, including California, Oregon, Washington, Idaho, and Nevada (hereafter West Coast + WIMW). These states are chosen based on the diagnostic assessment in Section 3.2 and previous work showing the inland trajectories of ARs that make landfall in Northern California (Rutz et al., 2014). By comparing the performance of these two models, we aim to determine whether tree-ring based data outside of the SRW can help improve the reconstruction of the AREO.

For the two models, we use a leave-K-years-out cross validation to assess the skill of these models at predicting the AREO over the instrumental period. For each set of out-of-sample predictions, the entire elastic net regression is re-fit, including the penalization hyperparameters. We conduct the cross-validation using two K values ($K = 1$ and $K = 9$) over two time periods (1916–1983 and 1916–2018). The 1916–1983 time period is considered because the SPI reconstruction is based on varying calibration periods, with the earliest ending in 1983 (see Section 3.1). Prediction skill is quantified using the log-likelihood of the left-out years, which

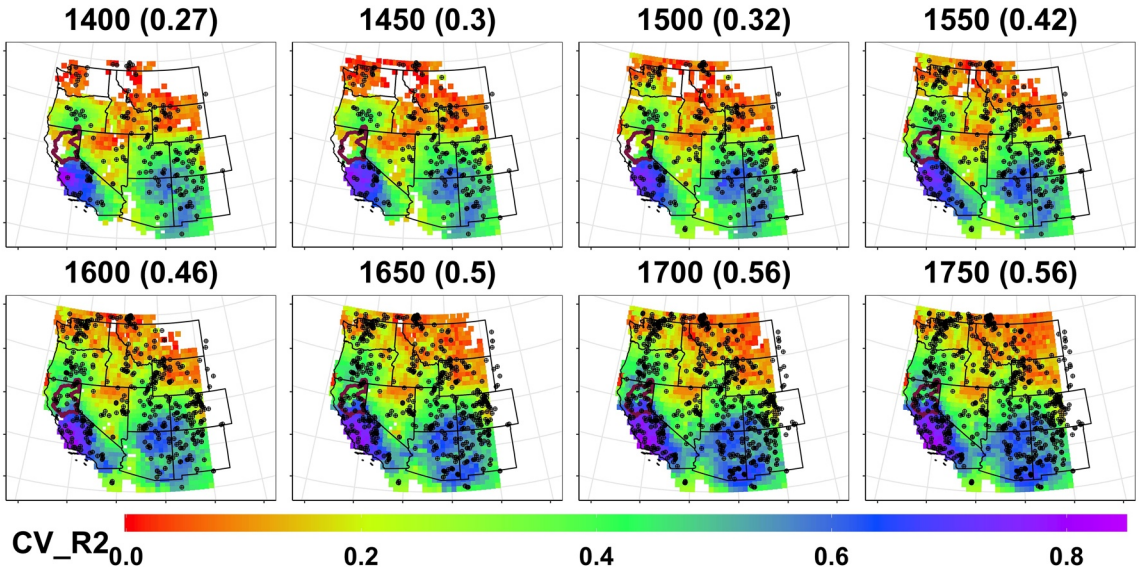

Figure 2. Cross-validated R^2 for the gridded, cold-season standardized precipitation index (SPI) based on leave-9-out predictions of the SPI between 1902 and 1983. Results are shown for reconstructions using tree-ring chronologies that extend back to various points in time. The locations of the chronologies used in the reconstructions back to the various points in time are shown as points. White areas: Reconstructions were not feasible due to the unavailability of tree-ring chronologies extending back to a given map's year of focus. Parentheses: Average R^2 within the SRW (violet boundary).

is an appropriate measure of model skill for the Poisson regression structure used here. We also report the rank correlation between observed and cross-validated AREO predictions.

After comparing the out-of-sample fit of the regression models over the instrumental period, we use the regression models to reconstruct the AREO back to 1400 CE and assess patterns of low-frequency variability using a wavelet analysis. To provide an additional validation of the reconstruction, we evaluate the distribution of the reconstructed AREO during pre-instrumental years (1840–1915) in which written records of past floods in the Sacramento Watershed are available (U.S. Army Corps of Engineers, 1999). We compare the distribution of the reconstructed AREO in flood and non-flood water years during this period and assess significance using a *t*-test. Large differences in the AREO distribution between flood and non-flood years suggests the reconstructed AREO is able to capture regional extreme events in the SRW.

We assess whether there are substantial differences between the reconstructions across the different regression models (SRW-only vs. West Coast + WIMW). In particular, we are interested in whether the models diverge in either the pre-instrumental or the instrumental records for large predicted AREO values, and if so, what drives the divergence. To support this assessment, we select the 20 years in which the two AREO reconstructions diverge by the greatest amount, but at least one of the reconstructions predicts a large AREO value (greater than one standard deviation of the instrumental period mean). For these years, we examine the spatial patterns of the gridded SPI to identify patterns that may cause the model reconstructions to diverge.

Finally, we consider how the model reconstructions change if they are conditioned on the reconstruction skill of the SPI being used as covariates. Specifically, we refit the models and repeat the intermodel comparison, but only using as covariates (1) SPI grid cells with a cross-validated skill above a minimum threshold and (2) SPI reconstructed only using tree-ring chronologies that extend all the way (rather than partially) back to 1400.

4. Results

4.1. Validation and Reconstruction of Cold-Season SPI

Figure 2 shows the cross-validated reconstruction skill (R^2) of the gridded, cold-season SPI. Skill is presented as the leave-9-out coefficient of determination between the reconstruction estimates and SPI observations

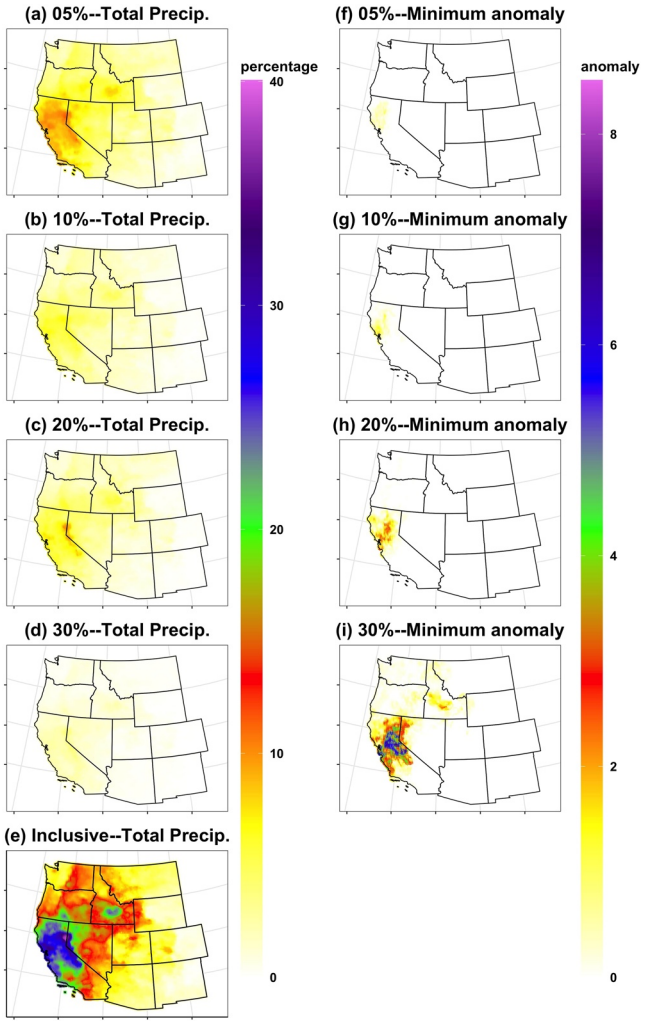

Figure 3. (a–d) The percentage of cumulative, cold-season precipitation delivered by mutually exclusive events when precipitation at 5%, 10%, 20%, and 30% of SRW stations exceeded the station-specific 99.5th percentile calculated for cold seasons between 1951 and 2013. (e) The percentage of cumulative, cold-season precipitation delivered during all events in which precipitation in at least 5% of SRW stations exceeded the station-specific 99.5th percentile (i.e., inclusive of all events in a–d). (f–i) The minimum precipitation amount delivered across the sets of extreme events, where different events can be selected for each grid cell and amounts are expressed as a (non-dimensional) factor of the daily mean value.

between 1902 and1983, and is shown for multiple versions of the reconstruction only using tree-ring chronologies that extend back to various points in time. Locations of these chronologies are also shown.

Several insights emerge from Figure 2. First, the reconstructions that extend back to 1400 CE are skillful in multiple regions of the western United States, including southern and central California, central Oregon, and across much of the Southwest in Arizona, New Mexico, Colorado, and Utah. In some of these regions, including south-central California, R^2 values exceed 0.75, and in the most southern portions of the SRW, R^2 values exceed 0.4. Second, as additional tree-ring chronologies become available over the centuries following 1400, SPI reconstructions become more skillful, particularly in areas of Northern California. This transition to enhanced skill is most apparent when tree-ring chronologies that extend back to 1550 are included due to the unique precipitation sensitivity of blue oak records in Northern California, which only extend back to the mid-1500s (Williams et al., 2020a). Finally, regions in central Idaho and northern Nevada consistently exhibit a low level of reconstruction skill, explaining approximately 10%–20% of the historic variability. This holds even when reconstructions utilize a large number of available chronologies and only extend back to 1750. This last result has important implications for the reconstruction of SRW extremes using the West Coast + WIMW model, which will be discussed below.

4.2. Diagnostic Assessment of Western US Precipitation During SRW Extremes

In the SRW, 99.5th percentile values of daily precipitation exceed 100 mm/day at stations in the Sierra Nevada, while lower values occur across the Central Valley (see Figure 1). Based on these percentiles, we identify 126, 73, 57, and 23 (all mutually exclusive) days with extreme precipitation occurring across at least 5%, 10%, 20%, and 30% of the 37 stations, respectively. We note that 87%, 88%, 100%, and 100% of these days were associated with ARs, based on a catalog of daily AR landfalls (Gershunov et al., 2017) along the Northern California coastline between 37°N and 42°N (allowing for a 1-day lag between AR landfall and extreme precipitation). The extreme precipitation days were clustered into events (described in Section 3.2), with some events lasting up to 7 days. During these events, there was substantial precipitation delivered across the Western US (Figure 3). Regardless of the threshold on the number of stations, there are regions in the Sierra Nevada with 5%–10% of total cold-season precipitation associated with regional SRW extreme events (Figures 3a–3d). In addition, similar ranges of total cold-season precipitation are associated with all sets of extremes in certain areas of the WIMW, such as in the rain shadow of the Cascades, central Idaho, and northern Nevada. Importantly, if we include all days during events wherein at least 5% of the stations in the SRW crossed the threshold (i.e., all days considered in Figures 3a–3d), 25%–40% of the total cold-season precipitation is associated with SRW extreme events in regions of Northern California and parts of central Idaho (Figure 3e). This raises the potential that reconstructions of cold-season precipitation in regions beyond the SRW contain useful information about past SRW extremes.

The minimum precipitation delivered during SRW extreme events highlights similar locations (Figures 3f–3i), particularly as the criterion for extreme events grows more stringent (i.e., a higher percentage of stations crossing their 99.5th percentile). For instance, during events when 30% of stations in the SRW exhibit extreme precipitation, significant positive precipitation anomalies always occur in central Idaho and eastern

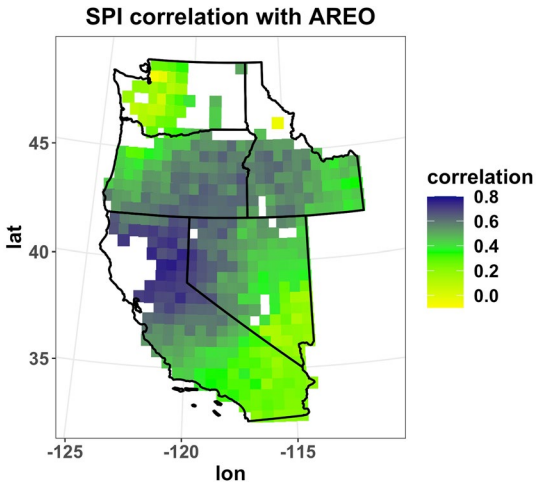

Figure 4. Correlation (Spearman) between the instrumental annual regional extreme occurrence (AREO) index and the gridded SPI reconstruction extended with observations (1916–2018 CE). Regions in white represent areas where reconstructions of SPI back to 1400 CE were not feasible due to the unavailability of tree-ring chronologies.

Oregon (Figure 3i). It is worthwhile to note that the spatial structures in Figures 3e and 3i resemble the path of an inland penetrating AR striking Northern California (Rutz et al., 2015), emphasizing the link between the path of these ARs and moisture delivered further into the continental interior. The results in Figure 3i suggest that as extremes in the SRW become larger in spatial extent, there is a higher likelihood that precipitation will be delivered to locations further inland in the WIMW. However, only ~8% of all extreme event days identified in this work fall into the set with 30% of stations exhibiting extreme precipitation. If fewer stations in the SRW experience extreme precipitation, minimum precipitation anomalies significantly above zero are only seen in Northern California (Figures 3f–3h). This suggests that as extreme events become more localized, locations in the WIMW do not always receive a precipitation signal from those events.

4.3. Intermodel Comparison and AREO Reconstruction

To systematically characterize regional extremes in the SRW, we define the AREO index as the cold-season count of the total number of individual extreme precipitation days across all stations. The AREO index ranges from 0 to 126 with a standard deviation of ~26, and its distribution is right-skewed. It is most strongly correlated with the monthly precipitation totals of December to February, with weaker correlations during other cold season months (Figure S1). Figure 4 shows the Spearman rank correlation between the instrumental AREO and the gridded tree-ring based SPI extended through 2018 with observations. The highest correlation coefficients occur in the SRW region, with values reaching 0.75, suggesting a strong connection between the reconstructed SPI and number of SRW extremes. High correlation values (>0.5) also extend into eastern Oregon, northwestern Nevada, and central Idaho, exhibiting a spatial structure that reflects the path of inland penetrating ARs (Rutz et al., 2015).

In the experimental design, two penalized Poisson regression models were developed for the AREO, each using data from the SPI over two different spatial domains (SRW-only or West Coast + WIMW). Figures 5a and 5b shows the selected regression coefficients from these two models (i.e., the β values in Equation 2). The penalized regressions select groups of SPI grid cells as covariates that tend to provide the best predictions of the AREO while minimizing collinearity among the covariate set, which explains the relatively sparse number of covariates selected. For the SRW-only model, the largest positive regression coefficients are located in the central-eastern portion of the basin (Figure 5a). These grid cells fall in the Sierra Nevada range and exhibit some of the highest correlations with the AREO (Figure 4). In the West Coast + WIMW model, the strongest coefficients are also found in the SRW (Figure 5b). However, there are also selected grid cells far outside of California, including south-central Oregon and central Idaho. These locations align with those regions emphasized in Figure 4.

Figure 5c shows the leave-one-out predictions of the AREO from the two models. Table 1 presents the log-likelihood and Spearman rank correlation over two sets of years (1916–1983 and 1916–2018) of observations and out-of-sample predictions for both leave-one-out and leave-nine-out cross-validations. We note that these results are based on models fit between 1916 and 2018 (including instrumental data), but the results are largely unchanged if the models are refit only using data from 1916 to 1983.

Overall, both models exhibit good skill, with cross-validated Spearman rank correlations ranging between 0.73–0.77 and 0.75–0.76 for leave-one-out and leave-nine-out predictions, respectively (Table 1). Few discrepancies emerge when comparing the SRW-only and West Coast + WIMW regression models over the instrumental period. The West Coast + WIMW model has slightly better log-likelihood and correlation scores when tested over 1916–2018, but the SRW-only model has slightly better scores when tested over 1916–1983. During extreme years, the differences between models are small. For instance, using the 10 largest and smallest AREO years, the mean squared error for leave-one-out predictions under the SRW-only model and the 1916–2018 evaluation period are 10.1 and 3.55, respectively; for the West Coast + WIMW model, these

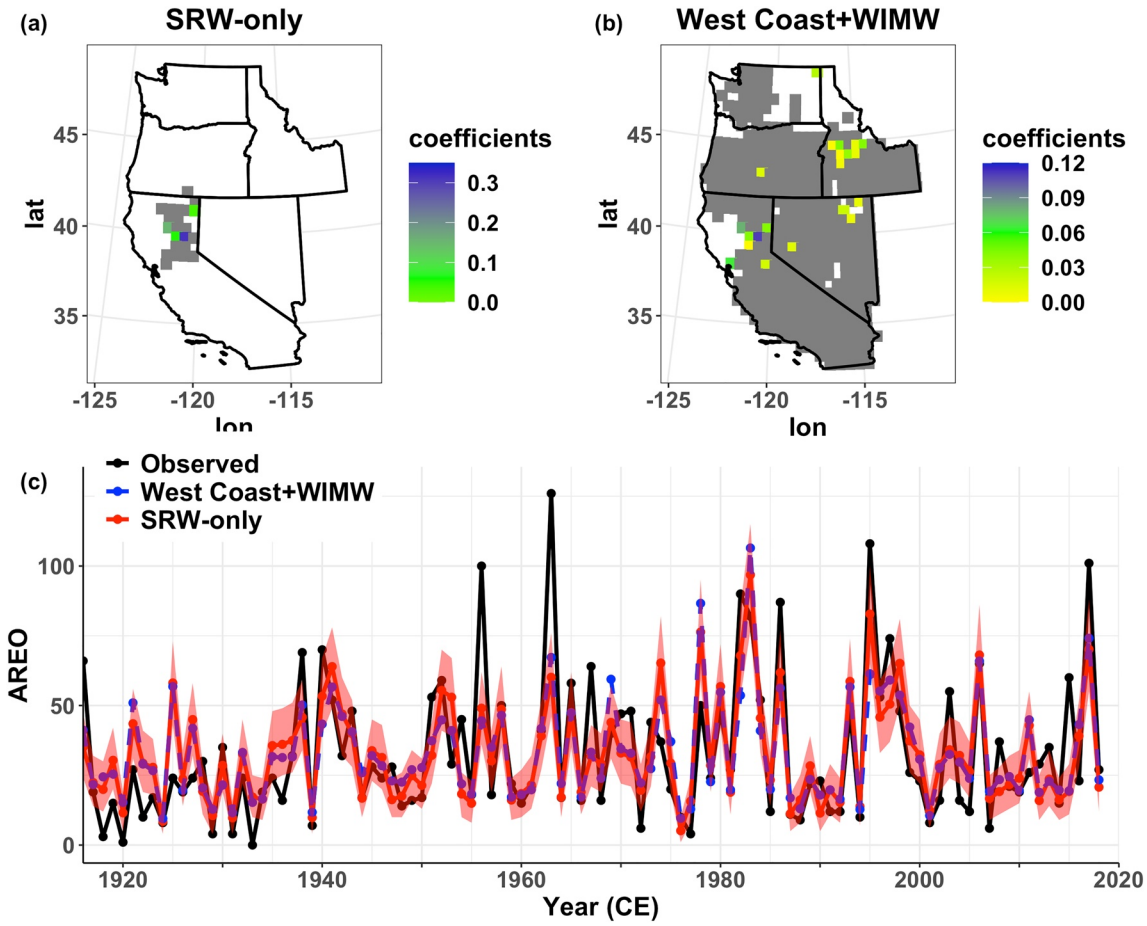

Figure 5. The regression coefficients of the elastic net Poisson regression for (a) the SRW-only and (b) the West Coast + WIMW models. Regions in gray have coefficients equal to 0, while regions in white were not included in the regression. (c) Time series of the observed and leave-one-year-out predicted AREO for the SRW-only and West Coast + WIMW models. The red faded region represents the 95% confidence interval of the Poisson distribution under the SRW-only model.

values are 10.71 and 3.91. Both models tend to underpredict the magnitude of some peak AREO values, particularly in 1956 and 1963, and overpredict others (1974 and 1978). However, the models are generally able to distinguish between low, average, and high AREO years. Overall, the two models perform similarly, which is not unexpected given their similar coefficient weighting of SPI data from the SRW (Figures 5a and 5b). The discrepancies that do emerge highlight how reconstructed SPI data outside of the SRW can modulate the signal from that region. This is explored further when examining the reconstruction of the AREO from both models, discussed next.

Table 1
The Log-Likelihood (and Spearman Correlation) Calculated for Leave-One-Out and Leave-Nine-Out Predictions Over Two Different Time Periods

	Leave-one-out		Leave-nine-out	
Model	1916–2018	1916–1983	1916–2018	1916–1983
SRW-only	−637.33 (0.75)	−421.74 (0.77)	−641.46 (0.75)	−430.53 (0.76)
West Coast + WIMW	−629.52 (0.76)	−456.93 (0.73)	−632.84 (0.76)	−457.42 (0.75)

Note. The regression models are developed using data from 1916-2018.

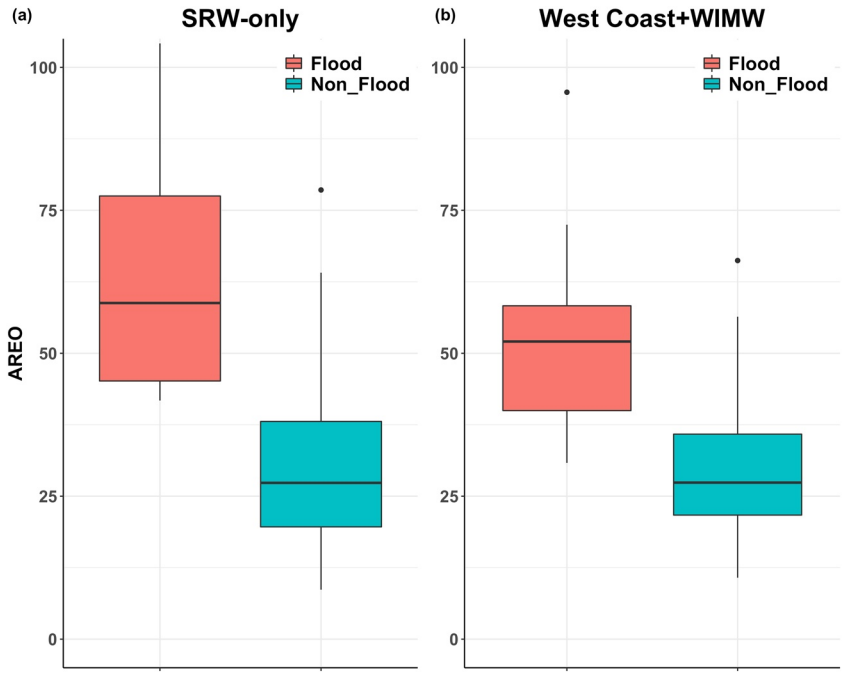

Figure 6. Box plots of the reconstructed AREO during flood years and non-flood years in the Sacramento River Watershed between 1840 and 1915 for the (a) SRW-only and (b) West Coast + WIMW models.

Figure 6 shows the distribution of the reconstructed AREO between 1840 and 1915 from the two models during years in which floods were and were not recorded in the SRW over that period. Flood years include 1850, 1853, 1862, 1868, 1878, 1881, 1896, 1890, 1907, and 1909 (U.S. Army Corps, 1999). Both models reconstruct significantly higher AREO values during known flood years compared to non-flood years (*t*-test *p*-values of 0.0005 and 0.001 for SRW-only and West Coast + WIMW models, respectively), with the mean AREO during flood years estimated to be approximately one standard deviation above the mean AREO in the instrumental period. The separation of median AREO values between flood and non-flood years is larger for the SRW-only model, but that model also predicts larger AREO values for some non-flood years. Conversely, the West Coast + WIMW model predicts a smaller separation in the central tendency of the AREO distribution across flood and non-flood years, but reduces the values of the AREO in some non-flood years.

Figure 7 shows the reconstructed AREO using the two regression models, as well as their difference. The reconstruction is extended back to 1400 CE. A high AREO threshold of 60 (one standard deviation above the mean AREO in the instrumental period of 1916–2018) is also superimposed on Figure 7. This threshold was chosen to isolate the largest AREO values in the historic record (1916, 1938, 1940, 1956, 1963, 1967, 1982, 1983, 1986, 1995, 1997, 2006, and 2017) and is used to highlight other extremes across the reconstruction.

Similar to their behavior in the instrumental record, the reconstructions from both models are consistent in terms of the timing of past extremes in the pre-instrumental record. Their correlation patterns against the SPI over the entire reconstruction period (1400–2018) are also quite similar (Figure S2). Both models identify a series of events that span from the mid to late 1500's to around 1700, and from the late 1700's to the early 1900's. At least one of the reconstructions (and often both) identifies peak AREO events (greater 60) in 1587, 1599, 1641, 1661, 1672, 1697, 1789, and 1825. There is a noticeable dearth of events between 1400 and 1550, a period reconstructed by Williams et al. (2020a) to have had remarkably little high-frequency variability in cool-season precipitation in the Sierra Nevada.

While the timing of AREO peaks is very similar between the two reconstructions, they do occasionally diverge (Figure 7c). The West Coast + WIMW model generally predicts lower AREO peaks as compared to the SRW-only model, as indicated by the tendency toward large positive differences. To better understand these differences, we selected 20 years with the highest discrepancy between the two reconstructions but also in which at least one of the reconstructions estimates the AREO to be higher than 60. We then clustered these

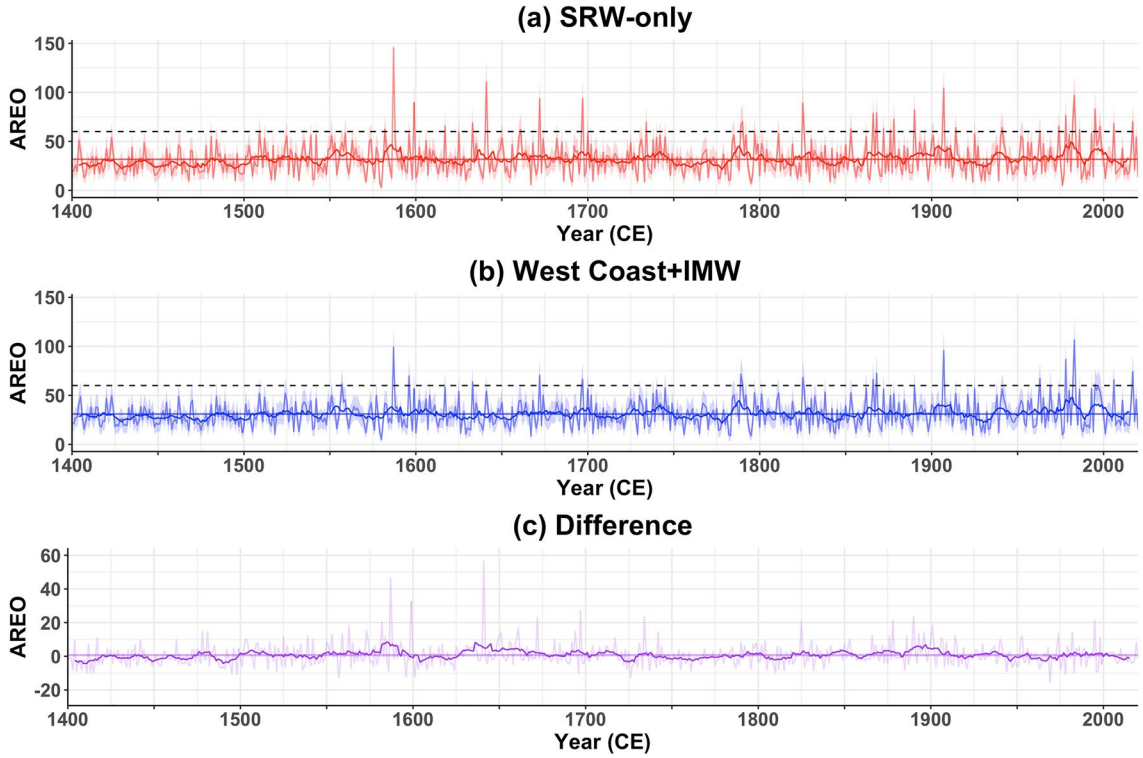

Figure 7. (a and b) The annual reconstruction of the AREO using the SPI from the two nested models. The annual reconstructions are also smoothed with a 10-year rolling average (bold). The faded region represents the 95% confidence interval of the Poisson distribution. The colored horizontal lines represent the mean reconstructed AREO of each model. The dashed horizontal like represents the threshold used to identify large AREO values. (c) The difference between the reconstructed AREO between the two models (SRW-only minus West Coast + WIMW). The colored horizontal line is fixed at 0, and the bold line shows a 10-year rolling average.

20 years of SPI data into three groups based on a visual inspection of their spatial patterns. Figure 8 shows composite maps of the SPI anomalies across these three groups of years (SPI maps for individual years are shown in Figure S3). The first group (Group a; Figure 8a) exhibits significant SPI anomalies along the West Coast, from Northern California through Oregon and into Washington (1582, 1587, 1599, 1641, 1672, 1697, 1876, and 1974). The second group (Group b) exhibits a more southerly track of positive SPI anomalies along all of California and into Nevada, with negative SPI anomalies further to the north (Figure 8b;

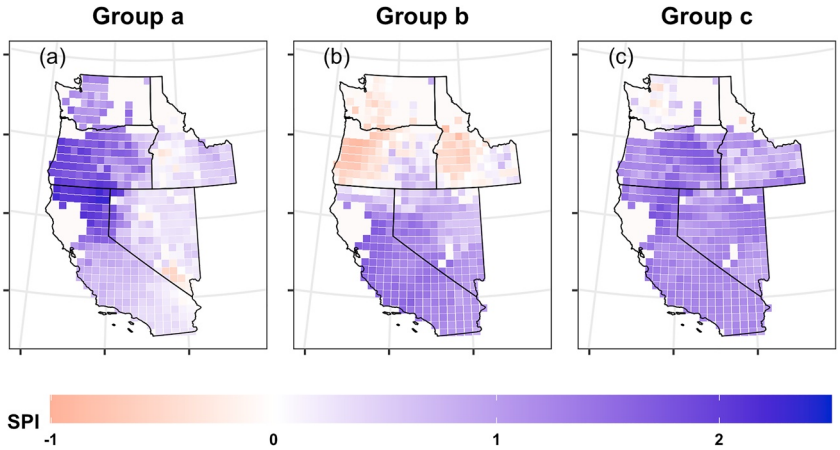

Figure 8. Composites of SPI anomalies for 20 years in which the reconstructions from the two models diverge by the greatest amount and AREO estimates from at least one of the models exceeds 60. These 20 years are first clustered into three groups (a–c; see text for description) based on their spatial pattern of SPI.

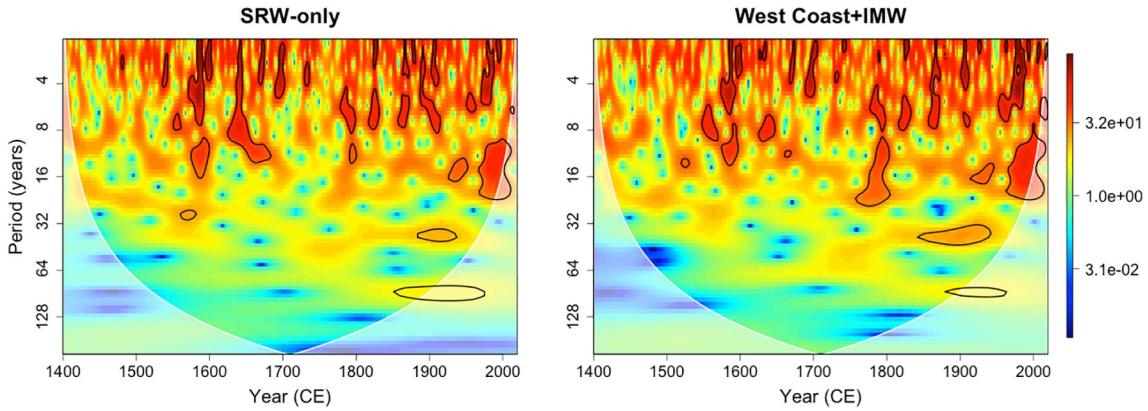

Figure 9. Wavelet power spectra for the SRW-only and the West Coast + WIMW AREO reconstructions. The areas within the shaded black boundary are significant at the 90% significance level.

1661, 1734, 1878, 1890, 1914, and 1998). The third group (Group c) exhibits positive and mostly uniform SPI anomalies across the entire West Coast and WIMW (Figure 8c; 1557, 1596, 1825, 1866, 1982, and 1995).

Two major insights emerge from Figure 8. First, in all instances, significant positive SPI anomalies are predicted across the Western US, not just in Northern California. However, the positions of these positive anomalies vary significantly across the groups, and are often coupled with neutral values or negative anomalies elsewhere. In Group (a) years when positive SPI anomalies suggest a coastal track for wet conditions, other regions of the WIMW (e.g., central Idaho) exhibit near-neutral or even negative SPI anomalies. During some of these years (1641, 1587, 1599, and 1697), the differences between the SRW-only and West Coast + WIMW models reach their highest levels (with SRW-only AREO predictions being much greater). In Group (b) years when SPI anomalies are most positive in the south, SPI anomalies in parts of Washington, Oregon, and Idaho are either neutral or negative. In both of these cases (Figures 8a and 8b), the SRW-only model always predicts larger AREO values than the West Coast + WIMW model. These results suggest that the SPI reconstruction likely captures multiple pathways for ARs delivering extreme precipitation to the SRW, and this causes the West Coast + WIMW model to predict lower values of the AREO compared to the SRW-only model.

The second insight relates to instances when the West Coast + WIMW model predicts larger AREO values compared to the SRW-model. These instances occur exclusively during Group (c) years when SPI anomalies are more uniformly positive across most of the West. Specifically, in some years, positive SPI anomalies in Northern California are weak compared to regions outside of California (1557, 1596), and in these years, the West Coast + WIMW model predicts larger AREO values (see Figure S3). Some years in the late 19th and early 20th centuries with known flood events exhibit a similar pattern (1862, 1938, 1983, and 1997; not shown), and the West Coast + WIMW model also predicts larger AREO peaks than the SRW-only model in those years. Therefore, there are instances when the tree-ring based reconstructions of SPI may be better able to identify extremes in the SRW using anomalies outside of California. However, this behavior is not consistent across most years, and the SRW-only model still predicts larger AREO values more frequently.

To characterize low-frequency variability within the two AREO reconstructions, Figure 9 shows the results of a wavelet analysis based on a Morlet wavelet (Torrence & Compo, 1998). The wavelet spectra are very similar across the SRW-only and the West Coast + WIMW reconstructions. In both reconstructions, the AREO exhibits significant low-frequency variability within the 2–8 year band. This mode of variability is most active between 1550–1650 and 1750 onwards, while it is reduced between 1650–1750 and noticeably absent prior to 1550. There is also a 10–20 year oscillation in the latter half of the 20th century in both time series, which also re-emerges in the West Coast + WIMW reconstruction directly prior to 1800 and to a lesser extent in the SRW-only reconstruction prior to 1600. This signal is consistent with the 13–15 year cyclicity in Western US cold-season precipitation evaluated by Johnstone (2011) and Williams et al. (2020a), and was shown by Dettinger and Cayan (2014) to coincide with an approximately 15-year periodic signal in

AR landfalls in Northern California. In addition, there is a 40-year signal in both reconstructions around the turn of the 20th century, but this oscillation is absent elsewhere in the time series.

Finally, as a sensitivity test we refit alternate AREO models based only on SPI grid cells for which the cross-validated R^2 exceeded 0.25. This prevents the AREO reconstruction from being influenced by areas where SPI reconstruction skill is poor such as northern Nevada and central Idaho (see Figure 2). With these areas removed, the new West Coast + WIMW model primarily selects as covariates SPI grid cells in the SRW and central Oregon (Figure S4), causing the SRW-only and West Coast + WIMW reconstructions to become more similar (Figure S5). In addition, we note that these alternate versions of the models perform marginally better than our primary AREO models that were developed without a screening on the SPI grid cells. For example, SRW-only leave-one-out predictions for key peak AREO years improve (1938, 1940, 1986, 1997, and 2017; see Figure S4), and the Spearman correlation and log-likelihood values reach 0.77 and −625.84 for the 1916–2018 period, which is a modest improvement over the values in Table 1 (0.75 and −637.33). In addition, we refit alternate AREO models using SPI reconstructions made only with RWI records that extend back to 1400. The leave-one-out Spearman correlation and log-likelihood values for this alternate SRW-only model are 0.7 and −797.8, similar to the values in Table 1, albeit with some loss of skill that is expected given that relatively few RWI chronologies extend back to 1400. Overall, the results of this latter sensitivity test add confidence that our final AREO reconstructions in Figure 7 maintain sufficient skill back to 1400 to be informative.

5. Discussion and Conclusion

This study explored the feasibility of reconstructing the interannual variability of extreme precipitation frequency in the SRW over the past several centuries. An analysis of instrumental-period precipitation across the Western US during SRW extremes highlighted key regions in California, the West Coast, and the WIMW (e.g., central Oregon and Washington, northern Nevada, central Idaho) that receive significant precipitation during these extreme events. This result underscored the possibility that precipitation-sensitive tree-ring chronologies from these regions might be useful in reconstructing SRW extreme precipitation events. To test this, we first created a gridded reconstruction of cold-season SPI across the West, which is an extension of the reconstruction presented in Williams et al. (2020a). This gridded reconstruction filtered the tree-ring chronologies into a spatially and temporally continuous data set useful for the reconstruction of SRW precipitation extremes, and serves as a stand-alone product useful for understanding past cold-season precipitation variability across the West. Results showed that the SPI reconstruction was skillful across much of the West back to 1400 CE, including southern portions of the Sacramento Valley and Central Oregon. Skill improved across the SRW when reconstructions began in 1550 CE. However, regions in the northern half of the West, including central Idaho, northern Nevada, and Washington, exhibited only modest skill throughout the reconstruction period.

We then developed an annual index of regional extremes (the AREO) and fitted penalized regression models using the reconstructed SPI within two nested regions (SRW-only vs. West Coast + WIMW). The two models performed similarly over the instrumental period, and were generally able to identify historical years with high, mid, and low occurrences of precipitation extremes. The models also were similar in their ability to separate flood from non-flood years in the 1840–1915 period, although the SRW-only model was arguably better at capturing extreme events. In the reconstruction, both models identified similar timing of extreme events over the last several centuries, but they diverged significantly in certain years.

The results from the pre-instrumental period lead to questions about why the West Coast + WIMW model generally under-predicted extremes compared to the SRW-only model, even though it did occasionally exhibit better AREO predictions in known extreme event years. The answer is likely related to two factors. First and most importantly, SPI reconstructions in central Idaho and northern Nevada exhibited relatively low skill, and this likely degraded the AREO reconstructions of the West Coast + WIMW model. In general, screening SPI covariates based on SPI reconstruction skill improved out-of-sample AREO predictions, and it reduced discrepancies between the SRW-only and West Coast + WIMW models. This highlights a limitation of the approach taken in this work that was not seen in a similar study in the Southwest US (Steinschneider et al., 2018): Cold-season precipitation totals in the continental interior that could be good proxies for the

likelihood of coastal extremes may not be reconstructed well enough for this purpose. Additional work should pursue improved reconstructions of cold-season precipitation in these regions, particularly central Idaho. The results of Figures 3e and 3i showed that instrumental precipitation in that region was particularly useful for distinguishing the most spatially expansive extremes impacting the SRW, and so improved cold-season precipitation reconstructions in central Idaho could prove critical for reconstructing the largest ARs impacting the SRW.

Second, the nonlinearity between patterns of SPI and extreme AREO values likely played a role in the West Coast + WIMW underpredictions. As discussed above, there is a diversity of spatial patterns in the SPI that can be associated with extreme AREO values. When comparing these patterns, there are many instances when positive SPI anomalies in some regions of the West Coast and WIMW associated with SRW extremes are counterbalanced by neutral or negative SPI anomalies in other key regions. Because the West Coast + WIMW model is a linear, additive model (on the logarithm of the mean AREO estimate) with positive coefficients in central Oregon, central Idaho, and northern and central Nevada (see Figure 5b), there is a tendency for positive SPI anomalies in some of these regions to be muted or canceled out by neutral or negative anomalies in the other regions. That is, the West Coast + WIMW model tends to smooth out the signal across a large regional domain, which may be poorly suited to the distinct spatial patterns that can emerge in the reconstructed SPI. This highlights a second limitation of the approach taken in this work that was not seen in Steinschneider et al. (2018): When trying to use tree-ring based proxies across the West Coast + WIMW to reconstruct coastal extremes, it may be necessary to use a nonlinear model better suited for a diversity of spatial patterns that could indicate extreme precipitation events. For instance, a neural network may be better able to classify extreme AREO events when SPI patterns suggest either a coastal track of wet conditions northward into Oregon and Washington or an inland track toward central Idaho. This effort is left for future work.

Although the reconstructions of extreme precipitation occurrences in the SRW presented in this work show promise, there are additional limitations to the analysis that require discussion. First, extreme precipitation is modeled using proxies based on moisture sensitive tree-ring chronologies that can only reflect a change in the likelihood of extreme precipitation occurrences but cannot identify those events precisely. Some of the AREO reconstruction's under- and over-predictions relative to instrumental and written historical records highlight this limitation. Therefore, the reconstructions developed in this work should be used in tandem with other paleoclimate evidence to better determine periods over the past millennium with increased and decreased frequency of extreme precipitation events. In addition, the reconstructions here cannot provide information on the magnitudes of individual extreme storms because radial tree growth is an integrated signal of total seasonal precipitation. This study was able to detect a tree-ring signal of the frequency of extreme precipitation events only because such events account for a significant proportion of total cold-season precipitation. The availability of tree-ring chronologies also diminishes significantly prior to 1400 CE, thereby limiting the reliability of reconstructions developed prior to this date. Finally, we have assumed stationarity in the relationship between the AREO and moisture proxies over centennial time scales, which could limit the fidelity of our reconstructions.

This work focused exclusively on the annual counts of extreme cold-season precipitation events in a single river basin in California and showed that tree-ring based proxies are indeed sensitive to these extreme events. Future work should explore the development of reconstructions of extreme event frequencies over the entire West Coast, using nonlinear regression models to identify the best spatial patterns of tree-ring based data that could inform reconstructions in each section of the coastline. This would help to synthesize the results presented here and in Steinschneider et al. (2018), and would provide a comprehensive analysis of past extreme events and the variability of landfalling ARs across the western coast of North America that would be of use to a wide range of water and environmental resource managers. Furthermore, the approach presented in this work should be extended to other regions, such as central Chile. That region has several similarities to Northern California, including: (1) a Mediterranean climate; (2) precipitation primarily delivered in the cold season; (3) a dominant influence of atmospheric rivers that impinge on a high mountain chain (the Andes) and cause heavy precipitation events (Guan & Waliser, 2015; Viale et al., 2018); and (4) an extensive network of tree-ring chronologies both in Chile and further inland in Argentina (Le Quesne et al., 2006; Morales et al., 2020; Mundo et al., 2011; Urrutia et al., 2011). Certain portions of the

western coast of the Iberian Peninsula also share some of these qualities (Eiras-Barca et al., 2018; Gallego et al., 2006; Natalini et al., 2016; Ramos et al., 2015). We hypothesize that because of these similarities, extreme precipitation reconstructions of similar skill to those presented in this work would be possible in parts of South America and possibly in southwestern Europe. This is left for future work.

Data Availability Statement

The data used in this analysis are publicly available, including daily station data gathered from the GHCN gauging network (https://www.ncei.noaa.gov/access/metadata/landing-page/bin/iso?id=gov.noaa.ncdc:C00861), as well as gridded precipitation data from the Livneh et al. (2015) data set (https://climatedataguide.ucar.edu/climate-data/livneh-gridded-precipitation-and-other-meteorological-variables-continental-us-mexico), the NOAA Climgrid data set (https://www.ncei.noaa.gov/metadata/geoportal/rest/metadata/item/gov.noaa.ncdc:C00332/html), and the CRU 4.04 data set (https://crudata.uea.ac.uk/cru/data/hrg/cru_ts_4.04/). The cold-season SPI reconstruction is available at https://www.ldeo.columbia.edu/~williams/wrr2021data/borkotoky_et_al_2021/. The RWI chronologies used to produce the SPI reconstruction are available at https://www.ldeo.columbia.edu/~williams/wrr2021data/rwi_data/.

Acknowledgments
The authors acknowledge support from NSF grants AGS1702273 and AGS1702184, a NOAA MAPP grant NA19OAR4310278, as well as the many tree-ring scientists over the past decades who have collected, processed, and made available their tree-ring data for studies such as this. In particular J. Littell shared data that he collected and measured from 18 sites the Pacific Northwest.

References

Akaike, H. (1974). A new look at the statistical model identification. *IEEE Transactions on Automatic Control*, *19*(6), 716–723. https://doi.org/10.1109/TAC.1974.1100705

Alexander, M. A., Scott, J. D., Swales, D., Hughes, M., Mahoney, K., & Smith, C. A. (2015). Moisture pathways into the U.S. intermountain west associated with heavy winter precipitation events. *Journal of Hydrometeorology*, *16*(3), 1184–1206. https://doi.org/10.1175/JHM-D-14-0139.1

Benito, G., & Thorndycraft, V. R. (2005). Paleoflood hydrology and its role in applied hydrological sciences. *Journal of Hydrology*, *313*(1–2), 3–15. https://doi.org/10.1016/j.jhydrol.2005.02.002

Cook, E. R., Anchukaitis, K. J., Buckley, B. M., D'Arrigo, R. D., Jacoby, G. C., & Wright, W. E. (2010a). Asian monsoon failure and megadrought during the last millennium. *Science*, *328*(5977), 486–489. https://doi.org/10.1126/science.1185188

Cook, E. R., Meko, D. M., Stahle, D. W., & Cleaveland, M. K. (1999). Drought reconstructions for the continental United States. *Journal of Climate*, *12*(4), 1145–1162. https://doi.org/10.1175/1520-0442(1999)012<1145:drftcu>2.0.co;2

Cook, E. R., Seager, R., Heim, R. R., Jr., Vose, R. S., Herweijer, C., & Woodhouse, C. (2010b). Megadroughts in North America: Placing IPCC projections of hydroclimatic change in a long-term palaeoclimate context. *Journal of Quaternary Science*, *25*(1), 48–61. https://doi.org/10.1002/jqs.1303

Cook, E. R., Seager, R., Kushnir, Y., Briffa, K. R., Büntgen, U., Frank, D., et al. (2015). Old world droughts and pluvials during the Common Era. *Science Advances*, *1*(10), e1500561. https://doi.org/10.1126/sciadv.1500561

Cook, E. R., Woodhouse, C. A., Eakin, C. M., Meko, D. M., & Stahle, D. W. (2004). Long-term aridity changes in the western United States. *Science*, *306*(5698), 1015–1018. https://doi.org/10.1126/science.1102586

Coumou, D., & Rahmstorf, S. (2012). A decade of weather extremes. *Nature Climate Change*, *2*(7), 491–496. https://doi.org/10.1038/nclimate1452

Daly, C., Neilson, R. P., & Phillips, D. L. (1994). A statistical-topographic model for mapping climatological precipitation over mountainous terrain. *Journal of Applied Meteorology*, *33*(2), 140–158. https://doi.org/10.1175/1520-0450(1994)033%3C0140:ASTMFM%3E2.0.CO;2

Dannenberg, M. P., & Wise, E. K. (2016). Seasonal climate signals from multiple tree ring metrics: A case study of *Pinus ponderosa* in the upper Columbia River Basin. *Journal of Geophysical Research: Biogeosciences*, *121*(4), 1178–1189. https://doi.org/10.1002/2015JG003155

Dettinger, M. D., & Cayan, D. R. (2014). Drought and the California delta—A matter of extremes. *San Francisco Estuary and Watershed Science*, *12*(2). https://doi.org/10.15447/sfews.2014v12iss2art4

Dettinger, M. D., Ralph, F. M., Das, T., Neiman, P. J., & Cayan, D. R. (2011). Atmospheric rivers, floods and the water resources of California. *Water*, *3*(4), 445–478. https://doi.org/10.3390/w3020445

Doss-Gollin, J., Farnham, D. J., Steinschneider, S., & Lall, U. (2019). Robust adaptation to multiscale climate variability. *Earth's Future*, *7*(7), 734–747. https://doi.org/10.1029/2019EF001154

Eiras-Barca, J., Lorenzo, N., Taboada, J., Robles, A., & Miguez-Macho, G. (2018). On the relationship between atmospheric rivers, weather types and floods in Galicia (NW Spain). *Natural Hazards and Earth System Sciences*, *18*(6), 1633–1645. https://doi.org/10.5194/nhess-18-1633-2018

Fritts, H. C. (1966). Growth-rings of trees: Their correlation with climate. *Science*, *154*(3752), 973–979. http://doi.org/10.1126/science.154.3752.973

Fritts, H. C. (1976). *Tree rings and climate*. London: Academic Press. Retrieved from https://www.sciencedirect.com/book/9780122684500/tree-rings-and-climate

Gallego, M. C., Garcia, J. A., Vaquero, J. M., & Mateos, V. L. (2006). Changes in frequency and intensity of daily precipitation over the Iberian Peninsula. *Journal of Geophysical Research*, *111*(D24), D24105. https://doi.org/10.1029/2006JD007280

Gershunov, A., Shulgina, T., Ralph, F. M., Lavers, D. A., & Rutz, J. J. (2017). Assessing the climate-scale variability of atmospheric rivers affecting western North America. *Geophysical Research Letters*, *44*(15), 7900–7908. https://doi.org/10.1002/2017GL074175

Guan, B., & Waliser, D. E. (2015). Detection of atmospheric rivers: Evaluation and application of an algorithm for global studies. *Journal of Geophysical Research: Atmospheres*, *120*(24), 12514–12535. https://doi.org/10.1002/2015JD024257

Guttman, N. B. (1999). Accepting the standardized precipitation index: A calculation algorithm. *Journal of American Water Resources Association*, *35*(2), 311–322. https://doi.org/10.1111/j.1752-1688.1999.tb03592.x

Harris, I., Jones, P. D., Osborn, T. J., & Lister, D. H. (2014). Updated high-resolution grids of monthly climatic observations – the CRU TS3.10 Dataset. *International Journal of Climatology*, *34*(3), 623–642. https://doi.org/10.1002/joc.3711

Hoerl, A. E., & Kennard, R. W. (1970). Ridge regression: Biased estimation for nonorthogonal problems. *Technometrics*, *12*(1), 55–67. http://doi.org/10.1080/00401706.1970.10488634

Hurvich, C. M., & Tsai, C.-L. (1989). Regression and time series model selection in small samples. *Biometrika*, *76*(2), 297–307. https://doi.org/10.1093/biomet/76.2.297

Johnstone, J. A. (2011). A quasi-biennial signal in western US hydroclimate and its global teleconnections. *Climate Dynamics*, *36*(3–4), 663–680. https://doi.org/10.1007/s00382-010-0755-9

Kapnick, S., & Hall, A. (2012). Causes of recent changes in western North American snowpack. *Climate Dynamics*, *38*(9), 1885–1899. https://doi.org/10.1007/s00382-011-1089-y

Lamjiri, M. A., Dettinger, M. D., Ralph, F. M., & Guan, B. (2017). Hourly storm characteristics along the U.S. West Coast: Role of atmospheric rivers in extreme precipitation. *Geophysical Research Letters*, *44*(13), 7020–7028. https://doi.org/10.1002/2017GL074193

Lepley, K., Touchan, R., Meko, D., Shamir, E., Graham, R., & Falk, D. (2020). A multi-century Sierra Nevada snowpack reconstruction modeled using upper-elevation coniferous tree rings (California, USA). *The Holocene*, *30*(9), 1266–1278. https://doi.org/10.1177/0959683620919972

Le Quesne, C., Stahle, D. W., Cleaveland, M. K., Therrell, M. D., Aravena, J. C., & Barichivich, J. (2006). Ancient *Austrocedrus* Tree-ring chronologies used to reconstruct central Chile precipitation variability from A.D. 1200 to 2000. *Journal of Climate*, *19*(22), 5731–5744. https://doi.org/10.1175/JCLI3935.1

Livneh, B., Bohn, T. J., Pierce, D. W., Munoz-Arriola, F. , B., Nijssen, B., Vose, R., et al. (2015). A spatially comprehensive, hydrometeorological data set for Mexico, the U.S., and southern Canada 1950–2013. *Scientific Data*, *2*, 150042. https://doi.org/10.1038/sdata.2015.42

McKee, T. B., Doesken, N. J., & Kleist, J. (1993). The relationship of drought frequency and duration to time scales. In *Paper presented at 8th Conference on Applied Climatology, 17–22 January, Anaheim CA*. Retrieved from https://climate.colostate.edu/pdfs/relationshipofdroughtfrequency.pdf

Meko, D. M., & Woodhouse, C. A. (2010). Application of streamflow reconstruction to water resources management. In M. K. Hughes, T. W. Swetnam, H. F. Diaz (Eds.), *Introduction. Dendroclimatology: Progress and prospects, developments in paleoenvironmental research series* (Vol. 11, pp. 230–261). Springer. Retrieved from https://doi.org/10.1007/978-1-4020-5725-0_8

Melvin, T. M., & Briffa, K. R. (2008). A "signal-free" approach to dendroclimatic standardisation. *Dendrochronologia*, *26*(2), 71–86. https://doi.org/10.1016/j.dendro.2007.12.001

Menne, M. J., Durre, I., Vose, R. S., Gleason, B. E., & Houston, T. G. (2012). An overview of the global historical climatology network-daily database. *Journal of Atmospheric and Oceanic Technology*, *29*(7), 897–910. https://doi.org/10.1175/JTECH-D-11-00103.1

Morales, M. S., Cook, E. R., Barichivich, J., Christie, D. A., Villalba, R., LeQuesne, C., et al. (2020). Six hundred years of South American tree rings reveal an increase in severe hydroclimatic events since mid-20th century. *Proceedings of the National Academy of Sciences of the United States of America*, *117*(29), 16816–16823. https://doi.org/10.1073/pnas.2002411117

Mundo, I. A., Roig Juñent, F. A., Villalba, R., Kitzberger, T., & Barrera, M. D. (2011). *Araucaria araucana* tree-ring chronologies in Argentina: Spatial growth variations and climate influences. *Trees*, *26*(2), 443–458. https://doi-org.proxy.library.cornell.edu/10.1007/s00468-011-0605-3

Natalini, F., Alejano, R., Vázquez-Piqué, J., Pardos, M., Calama, R., & Büntgen, U. (2016). Spatiotemporal variability of stone pine (*Pinus pinea L.*) growth response to climate across the Iberian Peninsula. *Dendrochronologia*, *40*, 72–84. https://doi.org/10.1016/j.dendro.2016.07.001

Palmer, J. G., Cook, E. R., Turney, C. S. M., Allen, K., Fenwick, P., Cook, B. I., et al. (2015). Drought variability in the eastern Australia and New Zealand summer drought atlas (ANZDA, CE 1500–2012) modulated by the Interdecadal Pacific Oscillation. *Environmental Research Letters*, *10*(12), 124002. http://dx.doi.org/10.1088/1748-9326/10/12/124002

Ralph, F. M., Dettinger, M. D., Cairns, M. M., Galarneau, T. J., & Eylander, J. (2018). Defining "atmospheric river": How the Glossary of Meteorology helped resolve a debate. *Bulletin of the American Meteorological Society*, *99*(4), 837–839. https://doi.org/10.1175/BAMS-D-17-0157.1

Ralph, F. M., Neiman, P. J., Wick, G. A., Gutman, S. I., Dettinger, M. D., Cayan, D. R., & White, A. B. (2006). Flooding on California's Russian river: Role of atmospheric rivers. *Geophysical Research Letters*, *33*(13), 1–5. https://doi.org/10.1029/2006GL026689

Ramos, A. M., Trigo, R. M., Liberato, M. L. R., & Tomé, R. (2015). Daily precipitation extreme events in the Iberian Peninsula and its association with atmospheric rivers. *Journal of Hydrometeorology*, *16*(2), 579–597. https://doi.org/10.1175/JHM-D-14-0103.1

Rutz, J. J., & Steenburgh, W. J. (2012). Quantifying the role of atmospheric rivers in the interior western United States. *Atmospheric Science Letters*, *13*(4), 257–261. https://doi.org/10.1002/asl.392

Rutz, J. J., Steenburgh, W. J., & Ralph, F. M. (2014). Climatological characteristics of atmospheric rivers and their inland penetration over the western United States. *Monthly Weather Review*, *142*(2), 905–921. https://doi.org/10.1175/MWR-D-13-00168.1

Rutz, J. J., Steenburgh, W. J., & Ralph, F. M. (2015). The inland penetration of atmospheric rivers over western North America: A Lagrangian analysis. *Monthly Weather Review*, *143*(5), 1924–1944. https://doi.org/10.1175/MWR-D-14-00288.1

Stahle, D. W., Cook, E. R., Burnette, D. J., Torbenson, M. C. A., Howard, I. M., Griffin, D., et al. (2020). Dynamics, variability, and change in seasonal precipitation reconstructions for North America. *Journal of Climate*, *33*(8), 3173–3195. https://doi.org/10.1175/jcli-d-19-0270.1

Stahle, D. W., Cook, E. R., Burnette, D. J., Villanueva, J., Cerano, J., Burns, J. N., et al. (2016). The Mexican Drought Atlas: Tree-ring reconstructions of the soil moisture balance during the late pre-Hispanic, colonial, and modern eras. *Quaternary Science Reviews*, *149*(1), 34–60. https://doi.org/10.1016/j.quascirev.2016.06.018

Steinschneider, S., Ho, M., Cook, E. R., & Lall, U. (2016). Can PDSI inform extreme precipitation?: An exploration with a 500 year long paleoclimate reconstruction over the U.S. *Water Resources Research*, *52*(5), 3866–3880. https://doi.org/10.1002/2016WR018712

Steinschneider, S., Ho, M., Williams, A. P., Cook, E. R., & Lall, U. (2018). A 500-year tree ring-based reconstruction of extreme cold-season precipitation and number of atmospheric river landfalls across the southwestern United States. *Geophysical Research Letters*, *45*(11), 5672–5680. https://doi.org/10.1029/2018GL078089

St. George, S., & Ault, T. R. (2014). The imprint of climate within Northern Hemisphere trees. *Quaternary Science Reviews*, *89*, 1–4. https://doi.org/10.1016/j.quascirev.2014.01.007

St. George, S., Meko, D. M., & Cook, E. R. (2010). The seasonality of precipitation signals embedded within the North American Drought Atlas. *The Holocene*, *20*(6), 983–988. https://doi.org/10.1177%2F0959683610365937

Swales, D., Alexander, M., & Hughes, M. (2016). Examining moisture pathways and extreme precipitation in the U.S. Intermountain West using self-organizing maps. *Geophysical Research Letters*, *43*(4), 1727–1735. https://doi.org/10.1002/2015GL067478

Tibshirani, R. (1996). Regression shrinkage and selection via the Lasso. *Journal of the Royal Statistical Society: Series B (Methodological)*, *58*(1), 267–288. https://doi.org/10.1111/j.2517-6161.1996.tb02080.x

Torrence, C., & Compo, G. P. (1998). A practical guide to wavelet analysis. *Bulletin of the American Meteorological Society*, *79*(1), 61–78. https://doi.org/10.1175/1520-0477(1998)079%3C0061:APGTWA%3E2.0.CO;2

Urrutia, R. B., Lara, A., Villalba, R., Christie, D. A., Le Quesne, C., & Cuq, A. (2011). Multicentury tree ring reconstruction of streamflow for Maule River watershed in south central Chile. *Water Resources Research*, *47*(6), 1–15. https://doi-org.proxy.library.cornell.edu/10.1029/2010WR009562

U.S. Army Corps of Engineers (USACE). (1999). *Post-flood assessment for 1983, 1986, 1995, and 1997 Central Valley, California: Chapter 2: History of flooding and flood protection*. Retrieved from https://deltarevision.com/maps/islands_floods_levees/sac_flood_history-detailed_usace.pdf

Vahedifard, F., AghaKouchak, A., Ragno, E., Shahriar, S., & Mallakpour, I. (2017). Lessons from the Oroville Dam. *Science*, *355*(6330), 1139–1140. http://doi.org/10.1126/science.aan0171

Viale, M., Valenzuela, R., Garreaud, R. D., & Ralph, F. M. (2018). Impacts of atmospheric rivers on precipitation in southern South America. *Journal of Hydrometeorology*, *19*(10), 1671–1687. https://doi.org/10.1175/JHM-D-18-0006.1

Vose, R. S., Applequist, S., Squires, M., Durre, I., Menne, M. J., Williams, C. N., et al. (2014). Improved historical temperature and precipitation time series for U.S. climate divisions. *Journal of Applied Meteorology and Climatology*, *53*(5), 1232–1251. https://doi.org/10.1175/JAMC-D-13-0248.1

Williams, A. P., Anchukaitis, K. J., Woodhouse, C. A., Meko, D. M., Cook, B. I., Bolles, K., & Cook, E. R. (2020a). Tree rings and observations suggest no stable cycles in Sierra Nevada cool-season precipitation. *Water Resources Research*, *57*(3), e2020WR028599. https://doi.org/10.1029/2020WR028599

Williams, A. P., Cook, E. R., Smerdon, J. E., Cook, B. I., Abatzoglou, J. T., Bolles, K., et al. (2020b). Large contribution from anthropogenic warming to an emerging North American megadrought. *Science*, *368*(6488), 314–318. https://doi.org/10.1126/science.aaz9600

Zou, H., & Hastie, T. (2005). Regularization and variable selection via the elastic net. *Journal of the Royal Statistical Society. Series B: Statistical Methodology*, *67*(2), 301–320. https://doi.org/10.1111/j.1467-9868.2005.00503.x